Tellus (1998), 50A, 26–41
Printed in UK – all rights reserved

TELLUS
ISSN 0280–6495

Fast, eastward-moving disturbances in the surface winds of the equatorial Pacific

By RALPH F. MILLIFF*, TIMOTHY J. HOAR and ROLAND A. MADDEN *National Center for Atmospheric Research, PO Box 3000, Boulder, CO. 80307, USA*

(Manuscript received 1 April 1997; in final form 18 September 1997)

ABSTRACT

A fast, eastward signal in the surface zonal winds of the equatorial Pacific ocean is identified in ERS-1 data that coincide with an intraseasonal tropical oscillation during the intensive observing period of TOGA COARE. The fast eastward event is compared with observations for the same time period from the TAO moorings at the equator. Similar events are identified in longer records of the ERS-1 and TAO data. A composite event is constructed and a lag-correlation analysis is used to infer basin-scale propagation speed. The fast eastward events in the ERS-1 data are consistent with signals in station surface pressure and station profile data quantified by Milliff and Madden and connected with first-baroclinic mode equatorial Kelvin wave propagation.

1. Introduction

In their paper identifying the Intraseasonal Tropical Oscillation (ITO) Madden and Julian (1972)† noticed a fast, eastward signal in the sea-level pressure (SLP) anomaly associated with slower eastward propagation in the equatorial troposphere of the equatorial Indian and Pacific Oceans. Milliff and Madden (1996) have recently identified a fast, eastward-propagating, signal in the troposphere of the equatorial Eastern Pacific that they associate with the far-field dispersion response to the ITO. Their analyses detected evidence of this feature of the ITO in SLP anomalies, station geopotential heights, and complex empirical orthogonal functions synthesized from geopotential height and zonal wind profiles for stations spanning the Eastern Pacific (i.e., Kanton Island in the West, and either Balboa or Howard Air Force Base in the East). A phase speed estimate of about 40 ms^{-1} from cross-spectral analyses was shown to be consistent with inferences drawn from linear-wave theory.

In this paper we document examples of fast, eastward signals in the equatorial Pacific in the surface zonal winds as sampled by the European Space Agency ERS-1 scatterometer. We examine the relationship between these fast, eastward signals in surface zonal winds and those in the SLP anomaly signal associated with the ITO.

The next section describes the ERS-1 sampling and data constraints. We focus on a representative fast eastward event that coincides with the Intensive Observation Period (IOP) of the Tropical Ocean Global Atmosphere (TOGA) Coupled Ocean Atmosphere Response Experiment (COARE) in the western equatorial Pacific from December 1992 through February 1993 (Webster and Lukas, 1992). Sampling artifacts in the ERS-1 dataset are discussed. A comparison with wind data from the TOGA Tropical Atmosphere Ocean (TAO) array of moored instruments is described. A composite fast, eastward signal is developed from eleven events identified in the ERS-1 record from January 1992

* Corresponding author.
† See also Madden and Julian (1994) for a review.

through June 1995. Finally, a candidate physical mechanism for the fast, eastward signals is discussed.

2. Data and methodology

The ERS-1 scatterometer operates aboard a polar-orbiting platform with an orbital plane inclined 8.6° (counter-clockwise for an ascending orbit) with respect to a line of longitude. The instrument returns swaths (500 km width) of radar scattering cross-section (σ_o) cells at 25 km spacing (Attema, 1991). The σ_o data are inverted via a geophysical model function to provide 10 m wind speed and direction at a nominal 50 km resolution within the swath. The development and accuracy of geophysical model functions for this inversion are subjects of current research and they are beyond the scope of this work (Wentz et al., 1984; Freilich and Dunbar, 1993; Stoffelen and Anderson, 1997). For our purposes, we consider the "rank-1" wind vector cell (WVC; i.e., the 50 km resolution cells within the swath) retrievals of the "value-added product" provided by NASA Jet Propulsion Laboratory (Freilich and Dunbar, 1993) to be good estimates of the true wind at 10 m in the equatorial Pacific.

2.1. *ERS-1 scatterometer coverage of the equatorial Pacific*

An example of the ERS-1 scatterometer retrievals for the tropical Pacific (20°N to 20°S, and 140°E to 280°E) for a typical 24-h period (17, January 1993), during the 35-day repeat orbit configuration, is depicted in Fig. 1a. The sampled region is scanned in a direction normal to the satellite orbital direction such that continuous swaths of WVC are retrieved. Swaths inclined from southeast to northwest (northeast to southwest) are sampled on ascending (descending) branches of the given orbits. On the sample day in Fig. 1a, the first swath of the 24-h period occurred on an ascending branch of the orbit near the eastern edge of the domain. Subsequent passes occurred at intervals of about 100 min, on ascending branches of consecutive orbits, marching westward across the domain with swath spacings on the order of 25° in longitude (e.g., from the first WVC in one swath to the first WVC in the next sampled swath). A 4-h interval separates the ascending passes from a sequence of descending passes over the domain. The ascending and descending swaths cross at a latitude of about 12°S during the 24-h period shown.

Missing data can occur at irregular intervals, either for a few swaths or for entire orbits as is evident from Fig. 1a. For example, data are missing from a portion of an ascending swath near 208°E, 12°S. Similarly, two missing descending swaths should have crossed the equator in the vicinities of 205°E and 230°E, respectively. Data dropouts can occur for a number of reasons, including failures of the model function algorithm to produce physically reasonable wind speeds or resolve directional ambiguities, contamination of the backscatter signal by rain effects on the surface, temporary disabling of the scatterometer instrument, etc.

Fig. 1b demonstrates that the ERS-1 coverage for the subsequent 24-h period (18, January 1993) divides the inter-swath spacings from the previous 24-h coverage into two unequal parts each. The new inter-swath spacings relative to the previous 24-h coverage (barring dropouts) are about 8° and 17° longitude. Fig. 1c demonstrates that the 17° spacings are then halved by the coverage in the third 24-h period (19, January 1993). This completes the so-called 3-day sub-cycle of the ERS-1 orbit. A fourth 24-h coverage map would overlap by more than half a swath width, the coverage in the first 24-h period shown here (17, January 1993; Fig. 1a). The overlap covers the western edge of each swath such that the sampling precesses westward until after about 35 d, an exact repeat orbit occurs. Notice that descending tracks from late in one 24-h period are crossed at the equator by ascending tracks from early in the subsequent 24-h period.

Our analyses are built upon longitude versus time representations of zonal winds from ERS-1 as exemplified in Fig. 2. The spatial domain spans the equatorial Pacific from 140°E to 280°E. The temporal domain covers 90 d from December 1992 through February 1993, coinciding with the TOGA-COARE IOP. Each WVC retrieved by the model function algorithm within 0.1° of the equator has been marked by a single dot in Fig. 2b. The tightest clusterings of dots in Fig. 2b occur in horizontal lines of adjacent WVC from within a single swath. Close inspection of Fig. 2b reveals a

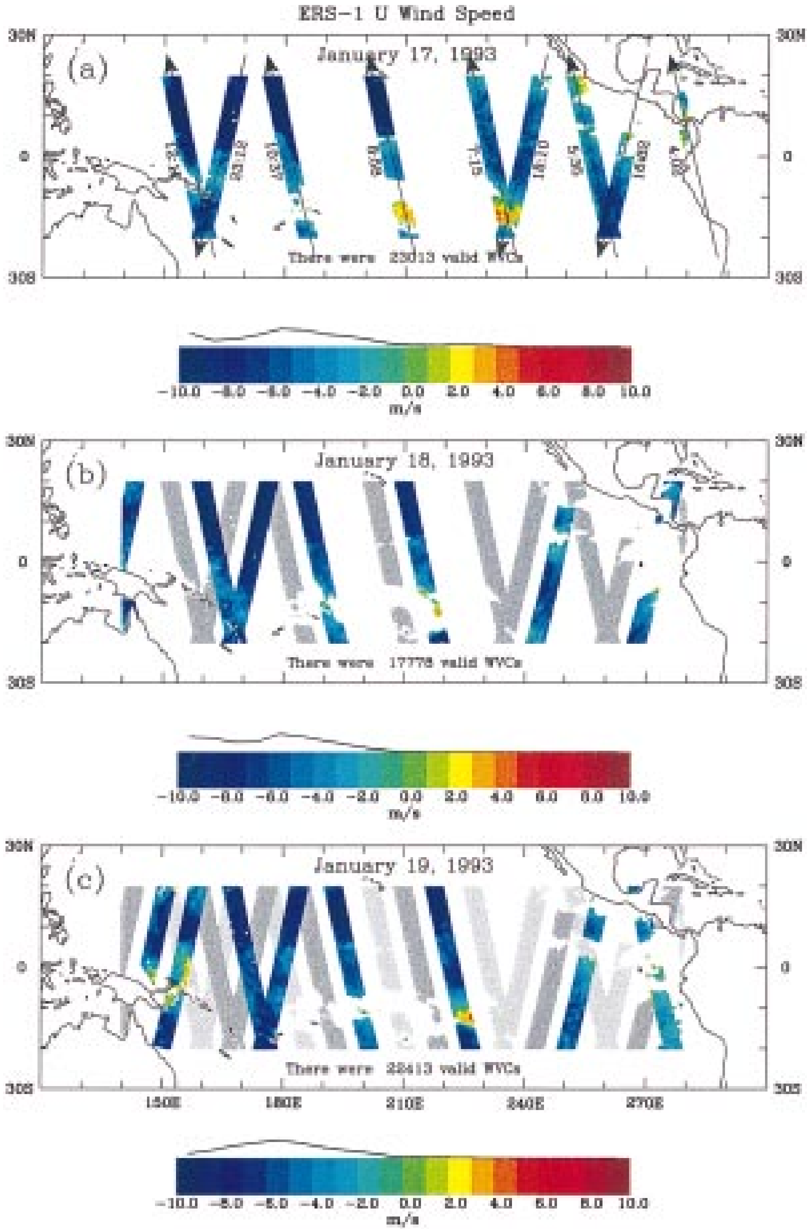

Fig. 1. Sample ERS-1 scatterometer coverage of the equatorial Pacific for three consecutive 24-h periods; 17–19 January 1993 (panels a–c). Wind vector cell (WVC) retrievals of the JPL value-added algorithm (Freilich and Dunbar, 1993), for the region 20°S to 20°N of the equatorial Pacific, are color coded according to zonal wind speed. The distribution of zonal speeds for each 24-h period is indicated above each color bar. The satellite direction (black arrows) and equator crossing times (UTC) for each pass on 17 January (panel a) are indicated. Data dropouts can occur within individual swaths and/or for entire swaths, as is evident for descending passes in the mid-Pacific (see text). The swaths sampled from the preceding 24-h periods (panels b and c) are indicated in shades of gray; lighter shade for older sampling. Panel c demonstrates typical ERS-1 scatterometer coverage of the equatorial Pacific for a 3-day sub-cycle of the 35-day exact repeat orbit configuration.

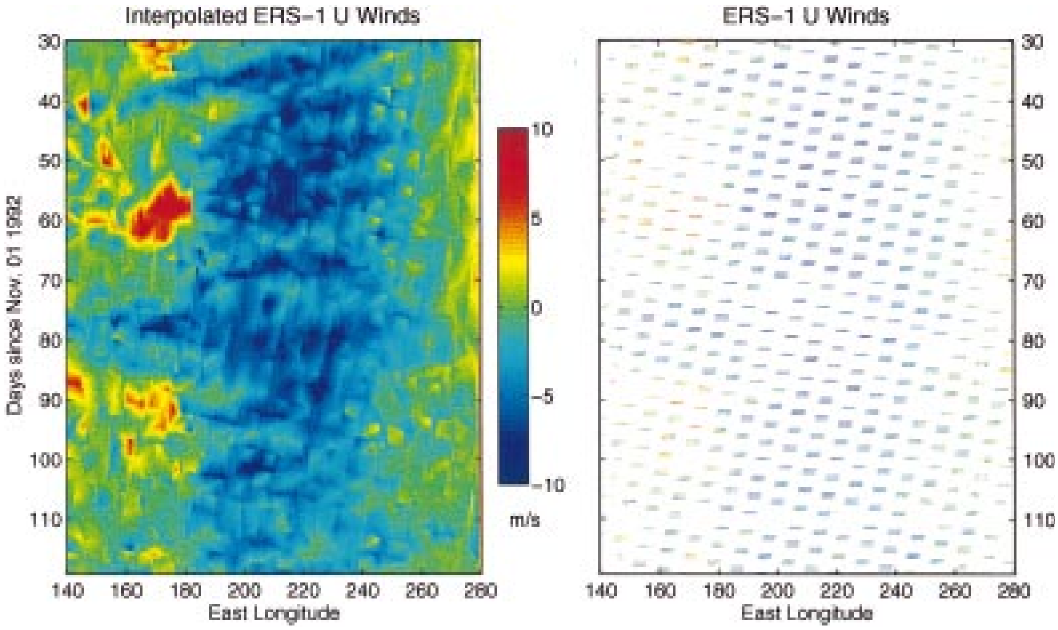

Fig. 2. Longitude versus time diagrams of (a) zonal winds, and (b) ERS-1 coverage of the Equatorial Pacific (140°E to 280°E) for the period 1 December 1992 (day 30, where 1 November 1992 is day 0) through 28 February 1993 (day 120). Zonal wind speeds are color-coded according to the colorbar; for the interpolated field in panel a, and for the WVC observations in panel b. Basin-scale propagating features are discussed in the text. The WVC observations in panel b have been bilinearly interpolated to a 0.5° by 1 h grid in an attempt to produce a continuous zonal velocity field in panel a. However, the ERS-1 sampling in x,t (panel b) results in an artifact that appears as a regular pattern of quadrilateral cells throughout the space-time domain in panel a. In panel b, a single color-coded dot occurs for every WVC retrieved from the ERS-1 observations. Closely-spaced horizontal lines of dots correspond to the satellite swaths. Adjacent in time pairs of swaths correspond to ascending (earlier) and descending (later) branches of the polar orbit as it revisits the Equatorial Pacific on a given day. Other regularities in the sampling scheme are related to the 3-day sub-cycle, and the 35-day exact repeat time of the ERS-1 orbit configuration (see text). Regions of missing data are evident, in particular for the Eastern Pacific (200°E to 270°E), between days 70 and 90.

number of swaths with at least a few missing WVC retrievals, as well as instances when entire swaths are missing (also evident in Fig. 1).

Descending and ascending swath pairs are apparent in Fig. 2b, with a slight westward progression of the later (ascending) swath in each pair. The westward precession of the sampling scheme in the 35 day repeat configuration is evident in Fig. 2b as tilted (upper-right to lower-left) columns of swath pairs (descending, then ascending) that span the entire time period. The tilted columns are separated by about 8.5°, and the swath-pairs along a tilted column are separated by about 3 d, consistent with the orbit configuration sub-cycle described above (Fig. 1).

In Fig. 2a we have interpolated the zonal wind part of the WVC retrievals indicated in Fig. 2b. Blue regions are indicative of easterly winds at the surface, yellow and red indicate westerly winds. The interpolation product depicted in Fig. 2a results from a bilinear interpolation to a 0.5° by 1-h (x,t) grid. Grid dimensions were selected to maximize the influence of each independent sample (i.e., each WVC) while providing for similar numbers of intervals in x and t as required by the interpolation algorithm (Akima, 1978). There is evidence of the ERS-1 sampling idiosyncrasies in Fig. 2a that overlay the geophysical signals of interest; note the regular patterns of steep upper-right to lower-left slopes that correspond to the westward precession of the sampling scheme (tilted columns) described above.

We attempted to identify and separate sampling artifacts from geophysics by means of a two-dimensional Fourier transform of the x,t space (Fig. 2a) into amplitude and phase spectra in frequency, wavenumber space (ω,k). The hope was that the (ω,k) spectra could be selectively filtered according to the sampling scheme parameters (e.g., 8.5° longitude between tilted columns, 3-day sub-cycle, etc.). Complications due to non-periodicity, non-stationarity, and possibly spectral leakage, prevented a clean deconvolution such that the back-transform of the filtered spectra ($\omega,k \rightarrow x,t$) retained residuals of the original sampling artifact.

Another approach is to explore interpolation techniques in (x,t) that are more sophisticated than the simple bilinear interpolation used to create Fig. 2a. We report in the Appendix on our experiments with a technique due to Jones and Zhang (1997). Parameters of the sophisticated interpolation scheme can be selected to remove more of the sampling artifact than in Fig. 2a (see Appendix). However, the geophysical interpretation we put forward here is independent of the interpolation scheme used, and we can refer to Fig. 2a for the purposes of the following discussion.

2.2. *Scatterometer winds during TOGA-COARE IOP*

There is an obvious large-scale difference in Fig. 2a between the eastern Pacific region (180°–260°) characterized by persistent easterly winds and the western Pacific region (140°–180°) that exhibits intermittent strong westerly events of about 10-day duration and 30-day separation. A closer look at the easterlies in the eastern Pacific reveals coherent bands (darker blue) that span the region. Beginning on day 30 and ending around day 70, there is a sequence of 4 or 5 bands tilting upper-right to lower-left indicating westward propagation. Phase speed estimates from the slopes of the westward propagating features are in the neighborhood of 5 to 7 ms^{-1}. These signals are consistent with symmetric (in pressure), equatorially-trapped Rossby waves (Matsuno, 1966). They have been described in detail, based on 850 hPa data, by Kiladis and Wheeler (1995) during some of the same time period investigated here.

Between days 70 and 80 in Fig. 2a, the sequence of westward-propagating equatorial Rossby wave features in the Eastern Pacific is interrupted by a domain-scale signal in the easterlies that propagates rapidly eastward (i.e., well past the dateline by day 80). A constant phase speed line corresponding to 40 ms^{-1} fits well with the slope of this feature in Fig. 2a, consistent with phase speed estimates from independent data in Milliff and Madden, 1996. In the following we will focus upon eastward phase speeds of this magnitude, and we will link the fast, eastward signal with a well-documented ITO event during the TOGA-COARE IOP (Nakazawa and Shibata, 1995). By day 90 a westward-propagating signal has been restored in the easterly winds between 180° and 250°E (Fig. 2a), albeit weaker than the signal in the sequence prior to day 80.

Fig. 3 is a longitude (0°–360°) versus time (days since 1 November 1992) diagram of the 200 hPa velocity potential or χ anomaly distribution along the equator. The estimates of χ are taken from a derived product available in the European Center for Medium Range Weather Forecasting (ECMWF) analyses, given twice daily at T42 resolution. Long-term means for 00 UTC and 1200 UTC have been subtracted to yield the anomaly field. Lorenc (1984) noted that the upper-level χ field provided a clear indicator of the ITO for the entire course of its global propagation. This is evident in Fig. 3 as the coherent feature in dark blue (i.e., a χ minima) that can be traced from 50°E near day 70, around the globe through day 110. A weaker ITO event is also evident from about 90°E near day 42 to the beginning of the ITO just described. The χ minima are deepest over the Indian and western Pacific oceans where the deep convection associated with the ITO is strongest.

The deep convection signal in the upper-level χ field in Fig. 3 occurs from about 50°E to 120°E, between days 70 and 80 where the timescale is the same as for Fig. 2. That is the time period over which the fast-eastward signal in the surface easterlies of the eastern Pacific is observed in the ERS-1 scatterometer data. If the longitude and time scales in Figs. 2, 3 are made to be consistent, a constant phase speed line drawn through the fast eastward signal in the ERS-1 data (Fig. 2) intersects the deepest convection signals in the Indian Ocean implied by upper-level χ anomalies in Fig. 3.

2.3. *Lag correlations*

The fast, eastward signal near day 80 in Fig. 2a is not the only one of its kind in the zonal wind

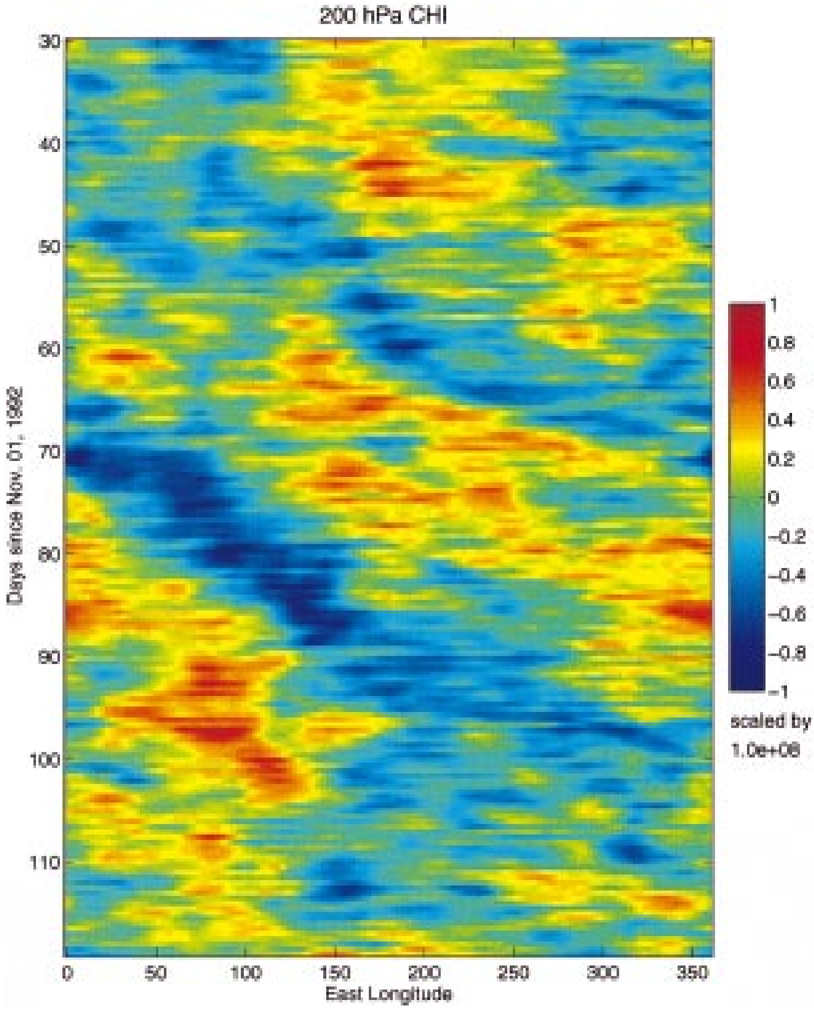

Fig. 3. Velocity Potential (χ) anomaly at 200 hPa as a function of longitude (x-axis) at the equator, and time (y-axis) in days since 1 November 1992. Units for χ are in m^2s^{-1}, and amplitudes are defined by the colorbar at right which has been scaled by a factor of 10^8. Each pixel corresponds to a 12-hourly anomaly of χ from a T42 resolution analysis produced by ECMWF, where either the 00 UTC or 1200 UTC long-term mean χ has been removed. Large amplitude, negative values for the χ anomaly correspond to strong convective episodes, most evident in the Indian and western Pacific oceans. The negative χ anomaly emanating from these regions is traceable around the globe and marks the propagation of the ITO.

retrievals from ERS-1 scatterometer data. In Fig. 4 we have extended the time period (y-axis) to 300 days but otherwise reproduced the format of Fig. 2. As before, the ERS-1 scatterometer data are interpolated to an (x,t) grid using a bilinear interpolation algorithm to create a continuous field. In the case of the longer 300 day time period, the grid increments are now 0.5° by 6 h. The fast, eastward signal, interrupting westward-propagating equatorial Rossby-wave signals shown in Fig. 2a, is reproduced near the top of Fig. 4a. A second, rapid eastward signal of similar slope occurs 125 days later (day 205). Both these events stand out in Fig. 4a because the eastward signal in the easterly wind belt (blue) is coherent from as far west as 140°E where episodes of strong

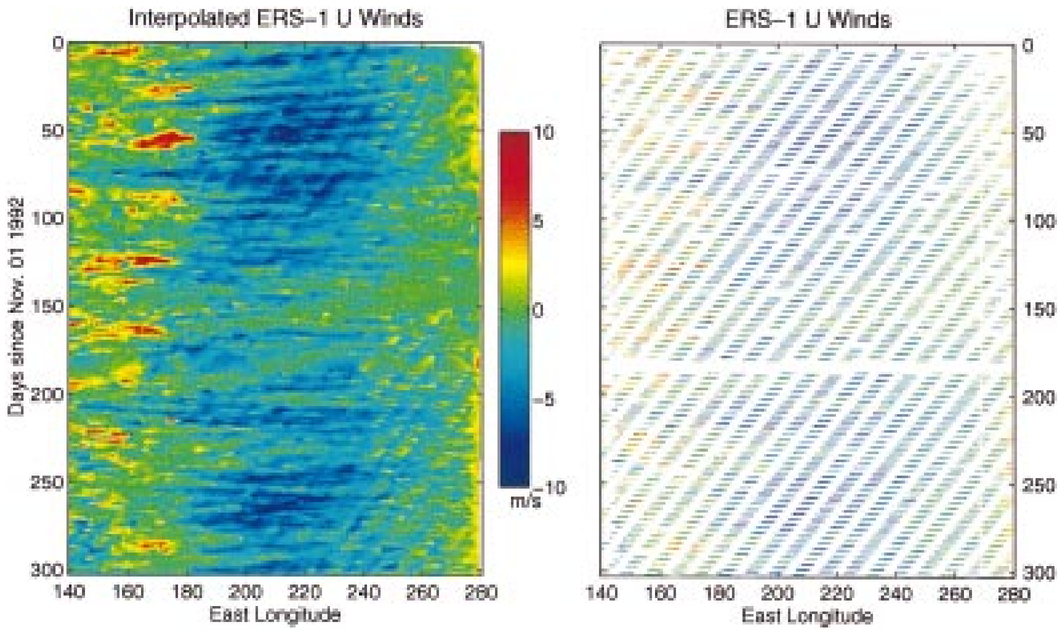

Fig. 4. Longitude versus time diagrams as in Fig. 2 for (a) zonal winds, and (b) ERS-1 WVC coverage of the same Equatorial Pacific domain, but now for the period from 1 November 1992 (day 0) through 31 August 1993 (day 303). The data were bilinearly interpolated to a $0.5^\circ \times 6$-h grid. The color scale for zonal wind speed is identical to Fig. 3.

westerly winds are more typical (yellow or red). The fast eastward events in the easterlies extend eastward well beyond the dateline. Between the two obvious eastward events there are candidate signals exhibiting fast, eastward propagation that are of lesser longitudinal extent, and are harder to separate from the spurious signals due to the ERS-1 sampling. If the fast eastward signals are uniquely associated with each ITO, then we should expect to see recurrences in Fig. 4a on time scales of 40 to 50 days.

In an effort to quantify this, a point-to-point lag correlation analysis was performed. The ERS-1 zonal winds were averaged over 10° longitude spans centered on 180° and 265°E. Correlation between these "stations" was computed as a function of temporal lag for the time period 6, January 1992 through 9, June 1995. Using a propagation speed estimate of 40 ms^{-1}, and the station separation (180° to 265°E), we can expect high lag-correlations representative of the fast, eastward signals exemplified in Figs. 2, 4 to produce a peak around 3-day lag (see also Milliff and Madden, 1996). In fact, the point-to-point lag correlations were everywhere small ($|r| \leqslant 0.2$), with the most prominent peak occurring at a temporal lag of 35 d. This coincides with the exact repeat time for the ERS-1 sampling that is manifest in Figs 2a and 4a as an artifact (tilted columns). The lag correlation analysis is therefore indicating that our bilinear interpolation procedure is not producing a uniformly continuous field of zonal velocities. For the time versus longitude organization of the ERS-1 dataset, a signal corresponding to the satellite sampling dominates point-to-point lag correlations (between 180°E and 265°E) that are generally weak over all temporal lags when 3.5 years of the ERS-1 record is considered.

2.4. *Composite lag correlations*

To better refine our estimate of the phase speed in the fast, eastward signal in the ERS-1 zonal winds we developed a composite from 11 fast, eastward events we could identify by eye in the longitude versus time record through June 1995

(1277 days). The 11 events were selected according to a set of subjective criteria that included requiring: clear eastward propagation over good x,t coverage in the ERS-1 record; enhanced easterly wind amplitudes; penetration of the easterly winds to the western Pacific (i.e., west of 180°E); and 30-day minimum temporal separation between events. Each fast, eastward event was registered in a 20-day temporal window for the region 140°E to 280°E. Rays corresponding to 40 ms^{-1} phase velocity were fit through the x,t data in the vicinity of each fast, eastward event identified in the record. The ray that projected upon the maximum easterlies was oriented such that the intercept at the western edge of the domain (140°E) corresponded to day 0. These (x,t) samples were then averaged at each x,t location to produce a composite event. A longitude versus time diagram of the composite fast, eastward event is shown in Fig. 5; with the 40 ms^{-1} ray superimposed. Note that artifacts of the ERS-1 sampling have been reduced substantially by the averaging procedure.

A space and time lag-correlation analysis of the fast, eastward composite was performed for the composite domain from 140°E to 279°E. Fig. 6 depicts the average lag-correlation surface $\bar{r}\,(\delta\lambda, \delta\tau)$ for lag correlations given by:

$$r\,(\delta\lambda, \delta\tau) = \frac{\dfrac{1}{N_t}\displaystyle\sum_{j=1}^{N_t} \hat{u}\,(i, j)\cdot\hat{u}\,(i+\delta\lambda, j+\delta\tau)}{\sigma_i\,\sigma_{i+\delta\lambda}}$$

where $(\delta\lambda, \delta\tau)$ are the spatial and temporal lags (in 1° and 1-day intervals), and N_t is the time period (20 days at 6-h resolution). The $\hat{u}$ are the zonal wind deviations from local mean zonal winds, and σ_i are the standard deviations (over time) at each spatial location, i.

The lag-correlation estimate in each (spatial lag, temporal lag) bin in Fig. 6 is an average of hundreds (large lags) to tens of thousands (small lags) of $(\delta\lambda, \delta\tau)$ pairs taken from the composite (Fig. 5). The lag-correlation averages are accumulated after a z-transform for each estimate to ameliorate a bias against large $r\,(\delta\lambda, \delta\tau)$ in untransformed data (Panofsky and Brier, 1968, p. 92). The significance of each lag-correlation estimate is a function of the number of independent spatial and temporal lag pairs that fall into the relevant bin. Not all of the $(\delta\lambda, \delta\tau)$ pairs in a given bin are independent. For example, if $\delta\lambda = 10°$, and $\delta\tau = 2$ days then the estimate of r (10, 2) contains contributions from

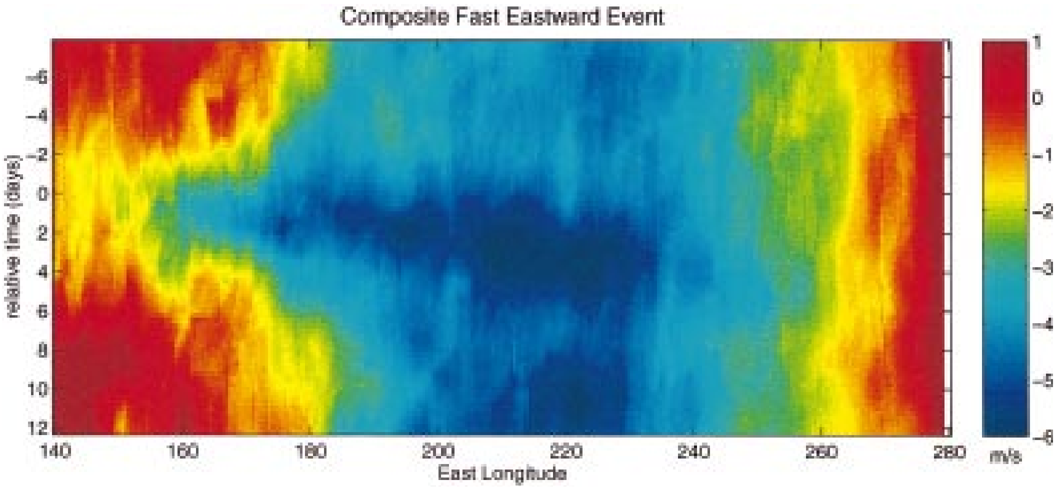

Fig. 5. (a) A composite fast, eastward event constructed from eleven 20-day segments of the ERS-1 record of zonal winds in the equatorial Pacific from 140°E to 280°E. The 11 individual events were identified by eye in the longitude versus time organization (bilinear interpolation) of the ERS-1 record through June, 1995. The individual events are registered to a 20-day temporal window by aligning in time the 40 ms^{-1} ray with maximum easterlies for each event. Such a ray intersects day 0 on the western edge of the composite. The averaging procedure used to construct the composite serves to reduce sampling artifacts that are evident in individual (x,t) sections (e.g., Fig. 2). The colorbar for zonal wind speed is different from those in Figs. 2, 4.

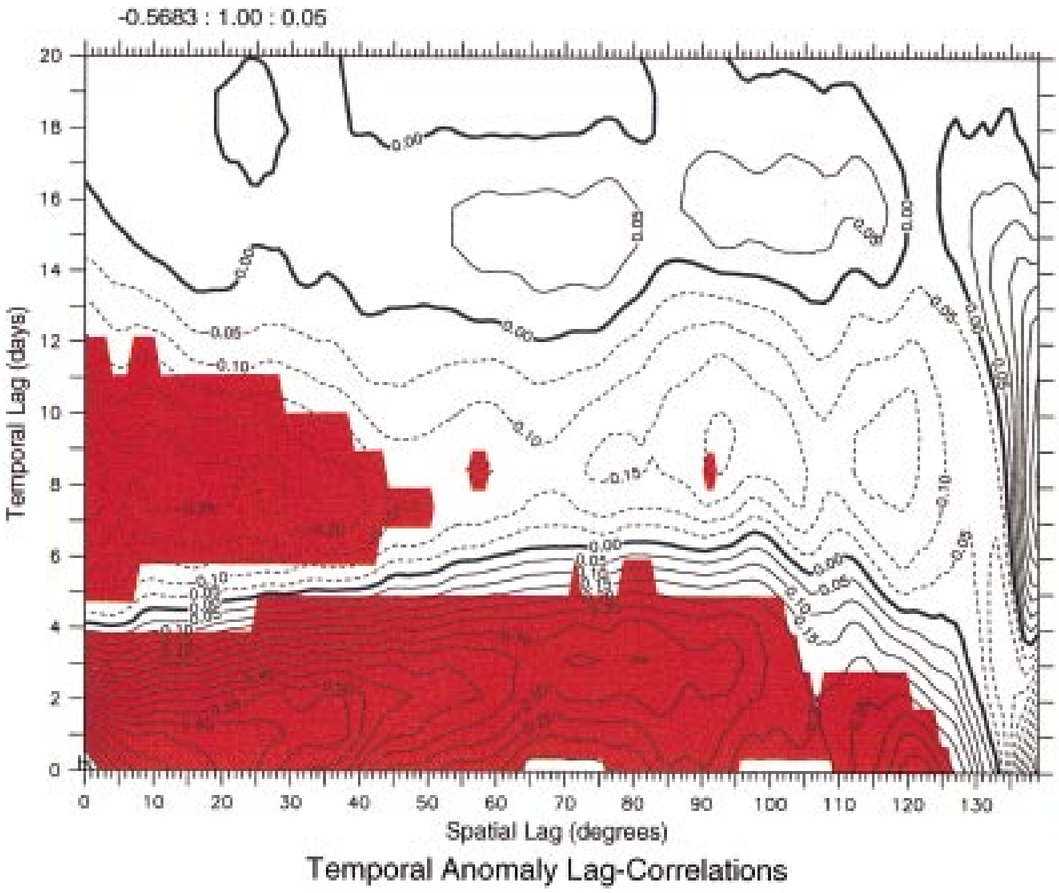

Fig. 6. Temporal anomaly, average lag-correlation surface for the fast, eastward zonal wind composite shown in Fig. 5. Temporal lags (in days, on the ordinate), versus spatial lags (in degrees longitude at the equator, on the abscissa) define lag-correlation bins that contain hundreds (large lags) to tens of thousands (small lags) of correlation pairs according to the (x,t) resolution in Fig. 5. Not all (spatial lag, temporal lag) pairs are independent (see text). Estimates of spatial and temporal autocorrelation scales have been used to estimate statistically significant (at the 95% level) correlation magnitudes which are highlighted in red. Statistical significance is not a rigorous concept in this context (see text). The field minimum, maximum, and contour interval are indicated in the upper left.

$\hat{u}$ (180°E, 1 day) $\hat{u}$ (190°E, 3 day) and $\hat{u}$ (180.5°E, 1 day) $\hat{u}$ (190.5°E, 3 days). If the autocorrelation function for $\hat{u}$ (180°E) is positive for distances greater than or equal to 0.5°, then these contributions to r (10, 2) contain redundant information that should be accounted for in computing the bin-average z-transform of the lag-correlation. We use estimates of the autocorrelations in space (10°) and time (5 days) to compute the average z-transform of the lag correlation in each $(\delta\lambda, \delta\tau)$ bin, using only pairs that are separated by at least 10° and 5 days. The bin averages are then back-transformed to yield $\bar{r}$ $(\delta\lambda, \delta\tau)$ in Fig. 6.

Similarly, we have used the same estimates of the autocorrelations in space and time to to compute the significance of the average lag-correlations. An average lag-correlation estimate is significantly different from $r\ (\delta\lambda, \delta\tau) = 0$, at the 95% level, for all the space and time lag bins highlighted in red in Fig. 6. Conversely, lag-correlation estimates in Fig. 6 that are not highlighted in red cannot be distinguished from

$r(\delta\lambda, \delta\tau) = 0$ in a statistically significant way at the 95% confidence level. The notion of statistical significance is not rigorous in this context since we have selected specific features from the ERS-1 dataset to build our composite. However, we can use the significance measure to exclude large amplitude (absolute value) lag-correlations that occur for the longest spatial lags in Fig. 6 (e.g., at days 0 and 8).

The strongest, significant, positive, average lag-correlations in Fig. 6 extend along a nearly straight ridge from the origin to a region around 90° spatial lag, and 3-day temporal lag. Not surprisingly, this corresponds to an eastward propagating signal at speeds in the vicinity of $40\,\mathrm{ms}^{-1}$. The correlation amplitude $\bar{r}$ (90°, 3 days) = 0.35 is not large, but it agrees with point-to-point lag-correlation estimates using historical data for surface pressure between Kanton Island (2.8°S, 171.7°E) and Balboa (9.0°N, 280.4°E) in Milliff and Madden (1996; see their Fig. 2, low-pass filter case). Milliff and Madden (1996) also demonstrate that point-to-point lag-correlations for surface pressures between Kanton Island and Howard AFB (8.9°N, 280.4°E) were as high as 0.65 using modern data (see their Fig. 4, low-pass filter case). However, the message from Fig. 6 is that relatively high lag-correlations are continuous for 3 days and over a 90° spatial extent. The absolute value of the average lag-correlation amplitude is somewhat arbitrary in that: it depends upon the selection of particular fast, eastward events from the ERS-1 record; it depends upon the size of the spatial and temporal window in the composite; and conservative estimates of spatial and temporal autocorrelations have been used to exclude redundant correlation estimates.

2.5. *TAO data*

Hourly-average surface wind (4-m anemometer height) observations are available from the TAO array of ATLAS moorings maintained in the tropical Pacific ocean by the NOAA Pacific Marine Environmental Laboratory (McPhaden, 1993). We use the winds from moorings located on the equator to create longitude versus time plots for time periods matching those in Figs. 2, 4. However, the hourly data from the TAO moorings were not amenable to the simple bilinear interpolation used for the ERS-1 data in the previous figures. The TAO moorings are widely separated along the equator relative to the WVC or even inter-swath spacings in the ERS-1 data. Conversely, hourly samples in the TAO data represent much finer temporal resolution than in the ERS-1 case which is closer to 12-hourly resolution at a given location (Fig. 1). The longitude versus time distribution of the zonal winds at the equator from the TAO moorings is thus distorted away from the uniformity required by bilinear interpolation algorithms. More sophisticated interpolation algorithms can operate on a distorted (x,t) distribution as we demonstrate in the Appendix. For now, we consider longitude versus time plots of the *daily* surface zonal winds from nine TAO moorings spanning the equatorial Pacific for: the TOGA COARE IOP in Fig. 7; and a 300-day period in Fig. 8 that is identical to the time period in Fig. 4 for ERS-1 (the daily winds derive from vector averages of the relevant 24 hourly values).

Comparing Fig. 7a with Fig. 2a, there is agreement in the timing and position of large-scale phenomena. For example, there is a coincidence in the transition from a regime dominated at all times by easterly winds at the equator in the Eastern Pacific (180° to 260°E) to a regime in the Western Pacific that is characterized by 5- to 10-day intervals of strong westerly winds. In both Figs. 2a and 7a, the easterly winds of the Eastern Pacific reach a maximum westward extent between days 70 and 80; crossing the dateline to 160°E. However, the daily TAO data do not recover sufficient detail in the Eastern Pacific to indicate clearly the propagation of features we noted in Fig. 2a. For example, in the region between 200°E and 230°E, details of the abrupt transition between days 70 and 80 from westward propagating Rossby waves to the fast, eastward signal are not as evident in Fig. 7a. Conversely, the longitude versus time format for the TAO data does not suffer from the same sampling artifacts we have noted in Fig. 2a. There are more isolated examples of artifacts in Fig. 7a near the western edge and at times when the data from a particular mooring begins or ends abruptly (e.g., see the coverage in Fig. 7b for the mooring at about 170°E). The essence of this comparison is unchanged in the examination of time versus longitude plots from the hourly TAO data as described in the Appendix.

Similarly, the comparison carries over to Figs. 4 and 8. The large-scale distinctions between per-

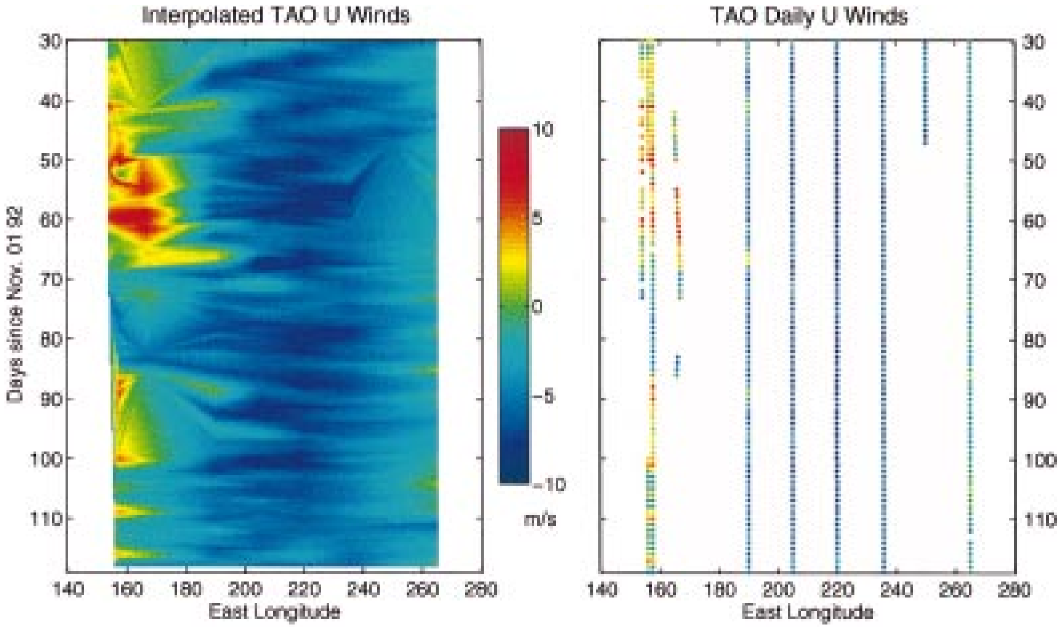

Fig. 7. Longitude versus time representations of the (a) daily zonal winds at 4 m, and (b) coverage for TAO data collected at Atlas mooring locations on the equator in the Pacific, and archived by the NOAA Pacific Marine Environmental Laboratory. The time period matches that of Fig. 2 (1 December 1992 through 28 February 1993). Zonal winds are recorded as hourly averages (obtained at 2 Hz over 6 min each hour) and then vector-averaged to produce the daily data used here. They have been bilinearly interpolated to a 0.5° by 1-h grid as in Fig. 2. The colorbar is identical to that of Fig. 2.

sistent easterlies in the Eastern Pacific and westerly wind events in the Western Pacific are comparable when the longer time period is considered. The fast, eastward events that span the domain from 160°E to 250°E are identifiable in Fig. 8a from the westward penetration of the easterly winds, but the changes in propagation direction across the Eastern Pacific are obscured. The sampling artifacts in Fig. 8 are of a very different character than those we have identified with the ERS-1 orbit configuration in Fig. 4.

Most of the artifact in Fig. 8 can be ameliorated by averaging the TAO zonal winds over 5 days (running average) and between the moorings at 2°N and 2°S (M. McPhaden, personal communication 1996). This aggregation smears the fast eastward signal in the eastern Pacific (3-day lag from 180°E to 260°E), but it delineates a fast, eastward slope in strong easterlies in the western Pacific (140°E–180°E) for the same times as the dominant eastward events in Fig. 4.

3. Discussion

We have alluded to a connection between deep convection near the initiation of the ITO in the equatorial Indian Ocean and the fast eastward signal in the easterly winds that span the Pacific, for 3 to 5 days, during the TOGA COARE IOP. Thus far, such a connection is only descriptive in that we cannot identify with the particular surface wind signal best seen in the ERS-1 data, a coincident surface pressure signal of the kind quantified by Milliff and Madden (1996).

Unfortunately, the TAO moorings do not record sea-level pressure (SLP). Another possibility is the detection of an inverted barometer effect in the sea-surface height (SSH) data from the TOPEX/POSEIDON altimeter observations (Fu and Pihos, 1994; Wunsch and Stammer, 1997). An estimate of the SLP amplitude of the fast, eastward signal of interest is on the order of 1 or 2 hPa. This corresponds to a 1 or 2 cm change in SSH

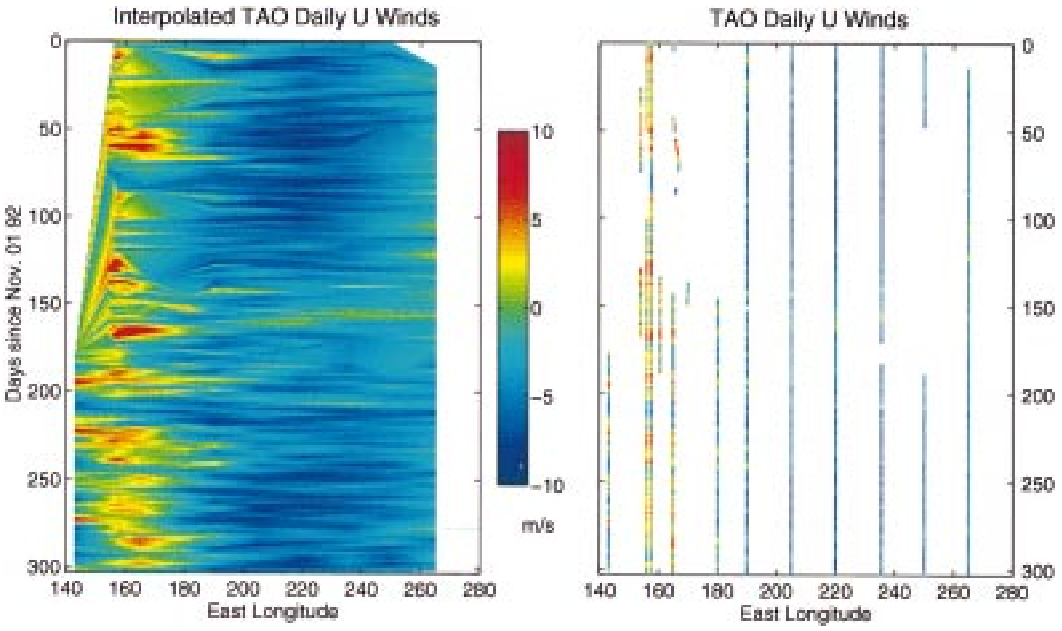

Fig. 8. Longitude versus time diagrams for (a) zonal winds, and (b) coverage as in Fig. 4, but for the daily TAO data.

for a perfect inverted barometer response. The TOPEX/POSEIDON data require averaging over more than 10 days to achieve a relative accuracy of this magnitude, thus obscuring the signal of interest that transits the Pacific basin in 3 to 5 days. The absolute accuracy of the TOPEX/POSEIDON data (given orbit and tidal corrections) is not better than 3 cm (Fu and Smith, 1996). Finally, the inverted barometer signal at a given location in the tropics is known to be contaminated by a response to remote wind-driving (Fu and Pihos, 1994).

To add to the description, we note that the phase speeds and the Pacific basin-scale spatial extent of the fast eastward signal are consistent with a theoretical Kelvin-wave response to an impulse forcing in the Indian Ocean. The ITO is thought to project almost exclusively on the first-baroclinic vertical mode structure of the equatorial troposphere. The change in the local wind O (5 m s^{-1}) is consistent with the equatorial Kelvin wave balance (see Gill, 1982, pg. 437) between zonal wind and perturbation pressure O (2 hPa). Theoretical phase speeds for first-baroclinic mode Kelvin waves, given parameterizations for typical vertical profiles of temperature and pressure, are on the order of 50 m s^{-1} (Matsuno, 1966; Gill, 1980; Milliff and Madden, 1996). The length scale associated with a phase speed of this magnitude and a time scale of 5 days, is about 250° of longitude, or enough to span the equatorial Indian and Pacific Ocean basins.

There are other descriptions in the literature of strong easterly surges associated with the ITO; some for the time period of interest here. McBride et al. (1995) set the synoptic context for the TOGA COARE IOP. They average (spatially) unfiltered zonal wind, from twice daily analyses, for grid locations occurring in each of 4 adjacent boxes (10° latitude by 30° longitude each) that span the region 10°S to 10°N, and 120°E to 180°E (see their Figs. 4, 5). Time series of the averaged zonal wind at 850 hPa demonstrate sharp maxima in easterly winds (-8 to -12 m s^{-1}) in mid-January (between days 70 and 80 on the timescale from Fig. 2) for each of the 4 boxes. The easterly maxima occur about one day later in the time series for the easternmost two boxes. McBride et al. (1995) link the maxima in the easterlies with ITO propagation and associated cloud features during TOGA COARE, but their focus is on the COARE region per se, and they do not consider possible remote effects of Indian Ocean convection. However, their Fig. 8 demonstrates the coincidence of deep convective clouds in the Indian Ocean with the fast eastward event in the zonal wind in the COARE region. In a complimentary study, Gutzler et al. (1994) set a larger-scale context for the TOGA COARE IOP. Time versus height plots of daily average wind from station data in the TOGA COARE region (their Fig. 10) demonstrate that the strongest surface easterlies during the IOP occur for a brief period in mid-January, associated with the eastward passage of the ITO.

Sheu and Liu (1995) document changes in precipitable water during the TOGA COARE IOP with a focus on westerly wind events. They average 850 hPa winds from 12-hourly ECMWF analyses between 2.5°S and 2.5°N. Their Fig. 3a depicts strong easterlies (about $10\ \mathrm{ms}^{-1}$) spanning the western Pacific from 130°E on day 76 (same timescale as our Fig. 2) to the dateline by day 80. The easterly surge separates in time two strong westerly wind events in the western Pacific as depicted in our Fig. 2. The connection between meridionally-averaged analysis winds at 850 hPa and surface winds from scatterometer observations is not necessarily a direct one. However, if the fast, eastward signal projects on a first-baroclinic mode equatorial Kelvin wave, we would expect to see evidence of a basin-scale signal above the planetary boundary layer, not unlike that depicted by Sheu and Liu (1995).

Kiladis et al. (1994) describe the large-scale circulation associated with deep convection over the western equatorial Pacific. They filter analysis field and out-going longwave radiation (OLR) data into 6–30 days and 30–70 days temporal bands, and then regress the filtered analyses against anomalous OLR within a reference region (e.g., the TOGA COARE intensive flux array region). For the ITO timescale (30–70 d), they note a surge in the 850 hPa easterlies of the central and eastern Pacific corresponding to deep convection over the TOGA COARE region. In addition, their Fig. 4 demonstrates strong easterlies over the TOGA COARE region for anomalous (low) OLR over the Indian Ocean. While these analyses hint at a connection between Indian Ocean convection and surges in the surface easterlies, the intent in Kiladis et al. (1994) was not the detection of fast eastward signals in the surface winds. These data are being revisited for that purpose (G. Kiladis personal communication 1997).

4. Summary

An example of fast eastward propagation (at about 40–50 ms^{-1}) of easterly zonal winds at the surface is observed to span the equatorial Pacific in a longitude versus time organization of ERS-1 data (Fig. 2) during the TOGA COARE IOP. Comparing this feature with a longitude vs time organization of 200 hPa χ anomaly field from ECMWF analyses (Fig. 3) connects the fast eastward event with deep convection in the Indian Ocean at the initial stages of an ITO event that is well-documented in the TOGA COARE IOP analyses (Nakazawa and Shibata, 1995; McBride et al. 1995). The fast eastward signal in surface zonal winds, and its association with the ITO, match features of a fast eastward signal defined, from multiple independent data sources, by Milliff and Madden (1996). In that paper, fast, eastward-moving surface pressure disturbances were linked to first-baroclinic mode Kelvin wave propagation.

The fast eastward signal in the surface winds interrupts a sequence of westward-propagating easterly wind events in the eastern Pacific (i.e., equatorial Rossby waves). The event during the IOP is shown to have counterparts in longitude versus time plots of surface zonal winds at the equator from scatterometer data for a period extending through 31 August 1993 (Fig. 4). Again, the westward-propagating equatorial Rossby-wave signals in the easterly winds provide a background signal that is interrupted by fast, eastward signals associated with the ITO.

A composite fast eastward event is constructed by averaging 11 events identified by eye in the ERS-1 record through June, 1995. Lag-correlation analysis is used to describe the composite event. A continuous ridge of relatively high correlation over 90° and 3 d confirms the existence of coherent eastward propagation in the surface easterly winds at about $40\ \mathrm{ms}^{-1}$ (Fig. 6).

Longitude versus time analyses of 4-m winds from the TAO mooring dataset at the equator (Figs. 7, 8) demonstrate abrupt changes in wind direction as far west at 140°E that coincide with the strongest examples of the fast, eastward signals in the scatterometer data. However, the TAO data are not distributed in an optimal way for the representation of propagation patterns in the windfield on the time and space scales of interest here.

While the detection of the fast, eastward signal does not depend crucially upon the interpolation technique in (x,t), the swath-based sampling for the scatterometer instrument of the polar-orbiting ERS-1 platform creates a spurious signal that pervades the longitude versus time diagrams constructed using a straightforward interpolation algorithm. The spurious signal can be damped substantially using sophisticated interpolation schemes demonstrated in the Appendix.

5. Acknowledgements

We thank Drs. R. H. Jones, G. Kiladis, M. McPhaden, G. Meehl, T. Nakazawa, and J-I. Yano for interesting discussions and helpful comments. RFM thanks Dudley Chelton for his hospitality at OSU, and Dennis Moore and Billy Kessler for their hospitality at PMEL. RFM is supported through a NASA Interagency Agreement for the NSCAT Science Working Team at NCAR. TJH is supported by the Geophysical Statistics Project at NCAR.

6. Appendix. Space, time interpolation of ERS-1 and TAO zonal winds

The ERS-1 data were interpolated with an S-PLUS (Statistical Sciences, 1993) routine *interp* which uses a modified version of the subroutine IDSFFT due to Akima (1978). The x,t data are parsed into a connected set of triangles to which is fit either a local, fifth-order polynomial, or a linear interpolation. We use the linear interpolation option. The triangulation method used by *interp* constrains the scales of the data axes to be

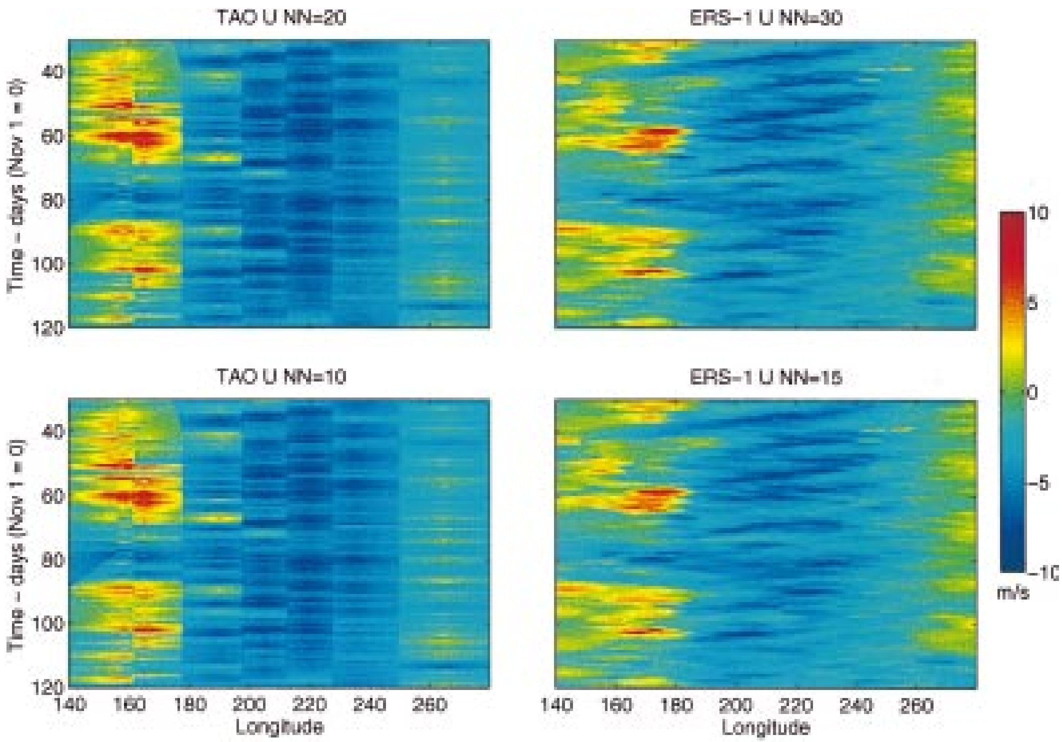

Fig. 9. Longitude versus time representations of surface zonal winds at the equator during the TOGA COARE IOP as measured by the TAO buoys (lefthand column) and the ERS-1 scatterometer (righthand column) and interpolated using a sophisticated space-time algorithm. Data coverage for the ERS-1 scatterometer is depicted in Fig. 2b. The *hourly* TAO data have been used here at the buoy positions indicated in Fig. 7b for the daily data. The "NN" heading for each panel indicates the number of "nearest-neighbors" used in the interpolation scheme.

within four orders of magnitude of each other. It is noted in the S-PLUS documentation, and it was our experience, that the interpolated results "appear stretched" if the data axes scales are very different at all.

The hourly TAO data did not lend themselves to interpolation of this sort. The relatively wide spatial sampling and fine temporal sampling resulted in a very peculiar triangulation. The interpolated field was, in fact, harder to interpret than a simple x,t scatter plot of the data.

The interpolation procedures for (x,t) data developed by Jones and Zhang (1997) treat separately the interpolation in space and time. Their methods are based on partial differential equations used to model irregularly sampled, space-time processes. A maximum likelihood technique is used to estimate a spatial-temporal auto-regressive model, which is then used for prediction at each of the desired grid points. The number of "nearest neighbor" points is determined by comparing the Akaike Information Criterion (AIC; Akaike, 1974) for the resultant models. The "best" model (smallest AIC) is then used for interpolation. The resultant field is not constrained to go through each observation, as it is with Akima's technique. Typically, the AIC, as a function of model order, decreases rapidly and then levels off. The models shown in Fig. 9 were chosen because they represent either the model at the "break point" of the AIC curve, or a model from the "best" category.

REFERENCES

Akaike, H. 1974. A new look at the statistical model identification. *IEEE Trans. Auto. Control* **19**, 716–723.

Akima, H. 1978. A method of bivariate interpolation and smooth surface fitting for irregularly distributed data points. *ACM Trans. on Math. Software* **4**, 148–164.

Attema, E. P. W. 1991. The active microwave instrument on-board the ERS-1 satellite. *Proceedings of the IEEE* **79**, 791–799.

Freilich, M. H. and Dunbar, S. 1993. A preliminary C-band scatterometer model function for the ERS-1 AMI Instrument. *Proceedings of the 1st ERS-1 Symposium – Space at the service of our environment*. Cannes, France. ESA-SP 359, 79–83.

Fu, L-L. and Pihos, G. 1994. Determining the response of sea level to atmospheric pressure forcing using TOPEX/POSEIDON data. *J. of Geophys. Res.* **99** (C12), 24 633–24 642.

Fu, L-L. and Smith, R. D. 1996. Global ocean circulation from satellite altimetry and high-resolution computer simulation. *Bull. Amer. Meteor. Soc.* **77**, 2625–2636.

Gill, A. E. 1980. Some simple solutions for heat-induced tropical circulation. *Q. J. Royal Met. Soc.* **106**, 447–462.

Gill, A. E. 1982. *Atmosphere-ocean dynamics*. International Geophysics Series, vol. 30. Academic Press, Inc., 662 pp.

Gutzler, D. S., Kiladis, G. N., Meehl, G. A., Weickmann, K. M. and Wheeler, M. 1994. The global climate of December 1992-February 1993. Part II. Large-scale variability across the tropical Pacific during TOGA COARE. *J. of Climate* **7**, 1606–1622.

Jones, R. H. and Zhang, Y. 1997. Models for continuous stationary space-time processes. Modelling longitudinal and spatially correlated data: methods, applications, and future directions, Gregoire, T. G. et al. (eds)., *Lecture Notes in Statistics* **122**, Springer-Verlag, New York, 289–298.

Kiladis, G., Meehl, G. A. and Weickmann, K. M. 1994. Large-scale circulation associated with westerly wind bursts and deep convection over the western equatorial Pacific. *J. of Geophys. Res.* **99** (D9), 18 527–18 544.

Kiladis, G. and Wheeler, M. 1995. Horizontal and vertical structure of observed tropospheric equatorial Rossby waves. *J. of Geophys. Res.* **100** (D11), 22 981–22 997.

Lorenc, A. C. 1984. The evolution of planetary-scale 200 mb divergent flow during the FGGE year. *Q. J. Roy. Meteor. Soc.* **110**, 427–441.

Madden, R. A. and Julian, P. R. 1972. Description of global-scale circulation cells in the tropics with 40–50 day period. *J. Atmos. Sci.* **29**, 1109–1123.

Madden, R. A. and Julian, P. R. 1994. Observations of the 40–50 day tropical oscillation. A review. *Mon. Wea. Rev.* **122**, 814–837.

Matsuno, T. 1966. Quasi-geostrophic motions in the equatorial area. *J. Meteorol. Soc. Japan* **44**, 25–43.

McBride, J. L., Davidson, N. E., Puri, K. and Tyrell, G. C. 1995. The flow during TOGA COARE as diagnosed in the BMRC Tropical Analysis and Prediction System. *Mon. Wea. Rev.* **123**, 717–736.

McPhaden, M. A. 1993. TOGA-TAO and the 1991–93 El Nino-southern Oscillation event. *Oceanography* **6**, 36–44.

Milliff, R. F. and Madden, R. A. 1996. On the existence and vertical structure of fast, eastward moving, disturbances in the equatorial troposphere. *J. Atmos. Sci.* **53**, 586–597.

Nakazawa, T. and Shibata, A. 1995. Variations of SST, convection, and water vapor associated with the Madden-Julian Oscillation during TOGA COARE. *Proceedings of the 1995 ADEOS/NSCAT Science Working Team Meeting*, 29 November–1 December 1995. Kyoto, Japan, (EEOC,NASDA publishers), pp. 113–124.

Panofsky, H. A. and Brier, G. W. 1963. *Some applications* *of statistics to meteorology*. The Pennsylvania State University Press, 223 pp.

Sheu, R-S. and Liu, G. 1995. Atmospheric humidity variations associated with westerly wind bursts during TOGA COARE. *J. of Geophys. Res.* **100** (D12), 25 759–25 768.

Statistical Sciences, 1993. *S-PLUS User's manual*, version 3.2. Seattle; StatSci, a division of MathSoft Inc.

Stoffelen, A. and Anderson, D. L. T. 1997. Scatterometer Data Interpretation: Measurement Space and Inversion. *J. Atmos. and Oceanic Technology*, in press.

Webster, P. J. and Lukas, R. 1992. TOGA COARE. The coupled ocean-atmosphere response experiment. *Bull. Amer. Meteor. Soc.* **73**, 1377–1416.

Wentz, F. J., Peteherych, S. and Thomas, L. A. 1984. A model function for ocean radar scattering cross sections at 14.6 GHz. *J. of Geophys. Res.* **89** (C3), 3689–3704.

Wunsch, C. and Stammer, D. 1997. Atmospheric loading and the oceanic "inverted barometer" effect. *Reviews of Geophysics* **35**, 79–107.